



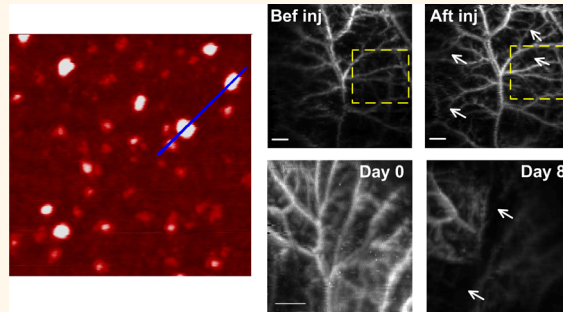
ARRCI
J

Early-Stage Imaging of Nanocarrier-Enhanced Chemotherapy Response in Living Subjects by Scalable Photoacoustic Microscopy

Liming Nie,^{*,†,‡} Peng Huang,^{‡,§} Weitao Li,^{‡,§} Xuefeng Yan,[‡] Albert Jin,[‡] Zhe Wang,[‡] Yuxia Tang,[‡] Shouju Wang,[‡] Xiaofen Zhang,[†] Gang Niu,[‡] and Xiaoyuan Chen[‡]

[†]State Key Laboratory of Molecular Vaccinology and Molecular Diagnostics & Center for Molecular Imaging and Translational Medicine, School of Public Health, Xiamen University, Xiamen 361102, People's Republic of China, [‡]Laboratory of Molecular Imaging and Nanomedicine (LOMIN), National Institute of Biomedical Imaging and Bioengineering (NIBIB), National Institutes of Health (NIH), Bethesda, Maryland 20892, United States, [§]Department of Biomedical Engineering, College of Automation Engineering, Nanjing University of Aeronautics and Astronautics, 29 Yudao Street, Nanjing 210016, People's Republic of China, and [†]Laboratory of Cellular Imaging and Macromolecular Biophysics, National Institute of Biomedical Imaging and Bioengineering (NIBIB), National Institutes of Health (NIH), Bethesda, Maryland 20892, United States. [#]L. Nie and P. Huang contributed equally to this work.

ABSTRACT Conventional evaluation methods of chemotherapeutic efficacy such as tissue biopsy and anatomical measurement are either invasive with potential complications or dilatory to capture the rapid pathological changes. Here, a sensitive and resolution-scalable photoacoustic microscopy (PAM) with theranostic nanoformulation was developed to noninvasively monitor the therapy response in a timely manner. Ultrasmall graphene oxide nanosheets were designed as both drug-loading vehicle and photoacoustic signal amplifier to the tumor. With the signal enhancement by the injected contrast agents, the subtle microvascular changes of the chemotherapy response in tumor were advantageously revealed by our PAM system, which was much earlier than the morphological measurement by standard imaging techniques. High tumor uptake of the enhanced nanodrug with Cy5.5 labeling was validated by fluorescence imaging. At different observation scales, PAM offered unprecedented sensitivity of optical absorption and high spatial resolution over optical imaging. Our studies demonstrate the PAM system with synergistic theranostic strategy to be a multiplexing platform for tumor diagnosis, drug delivery, and chemotherapy response monitoring at a very early stage and in an effective way.



KEYWORDS: early prediction · chemotherapy response · nanocarrier · photoacoustic microscopy · scalable imaging · graphene oxide · signal amplification

Although some anticancer drugs can inhibit tumor angiogenesis by inducing apoptosis and disrupting neovascular growth, many agents suffer from low drug loading, poor pharmacokinetics, and adverse systematic side effects.^{1,2} On the other hand, neovascularization in tumor microenvironment often produces insufficient imaging contrast, leading to inaccurate or delayed response monitoring.³ Recently, metallic nanoparticles, especially gold nanoconstructs, were extensively explored for drug delivery or imaging enhancement.^{4–6} In an *in vitro* model, functional peptide-coated gold nanoparticles

were used to particularly interface with cell receptors that determine progression or suppression of angiogenesis.⁷ Graphene oxide (GO) nanoparticles possessing two accessible surfaces with superlarge area are featured with low production cost and easy surface functionalization.^{8,9} They were reported to exhibit high drug loading and tumor uptake, and a strong photothermal effect on mice.^{10–12} Previously, graphene nanoparticles were primarily tested to generate higher photoacoustic (PA) signals than blood and proposed for *in vitro* targeted photothermal therapy and PA imaging.^{13,14} Nevertheless, they have neither been designed

* Address correspondence to nielm@xmu.edu.cn.

Received for review June 25, 2014 and accepted November 19, 2014.

Published online November 19, 2014
10.1021/nn505989e

© 2014 American Chemical Society

for simultaneous drug delivery and visualization improvement nor been explored for *in vivo* continuous PA monitoring of therapy response. Here, we developed a synergistic nanoplatform to overcome two challenges: simultaneously enhance drug delivery efficiency and boost PA contrast for improved visualization in one nanovehicle.

Noninvasive imaging techniques are imperative for early cancer detection and prediction of chemotherapeutic efficacy on tumors. However, most standard imaging techniques provide only morphological tumor information such as density, size, and shape. Positron emission tomography (PET) as a conventional imaging method can indirectly monitor therapy biochemical response by measuring metabolic activity and blood perfusion.^{15,16} Unfortunately, this radioisotope-dependent technique involves risky exposure to ionizing radiation.¹⁷ Magnetic resonance imaging (MRI) was also used to predict therapy response.^{18,19} The disadvantages of MRI include weak functional signals and suboptimum spatial resolution. Moreover, both PET and MRI employ costly and nonportable imaging equipment. Thus, it is greatly desired to develop a nonionizing and high-resolution imaging method capable of directly monitoring chemotherapy response in a timely manner.

Photoacoustic imaging (PAI) is an emerging optical imaging mode that can visualize various contrasts at millimeter depth with unprecedented sensitivity.^{20–22} By converting incident photons into ultrasound emission, PAI hybridizes the rich contrast of pure optical imaging and the high resolution of pulse-echo imaging in one modality.^{23,24} PAI, which relies on optical absorption distribution, is not affected by the autofluorescence in biological tissues commonly experienced by fluorescence imaging.²⁵ Inspired by these attractive merits, we have custom-built a sensitive photoacoustic microscopy (PAM) system to monitor and predict therapy response including tumor development and hemodynamics by different chemotherapeutic nanodrugs. Higher ultrasonic frequency, wider bandwidth, and finer step size increase spatial resolution, but decrease penetration depth and imaging speed, and *vice versa*. As a result, such versatile imaging scalability allows our PAM prototype to be used for multiple-scale imaging from diseased organs to local neovascularization changes with the same contrast origin.

GO nanoparticles can be functionalized by polyethylene glycol (PEG) to obtain high hydrophilicity in physiological environments.^{9,26,27} The surface fabrication can be realized by either covalent conjugation or noncovalent coating.^{10,28,29} In our experiment, we functionalized GO nanosheets by PEG in the first step and then linked them to Cy5.5 dye for fluorescence imaging. Afterward, a large amount of doxorubicin (Dox) was successfully loaded on the surface of a GO-PEG-Cy5.5 system *via* supramolecular $\pi-\pi$ stacking.

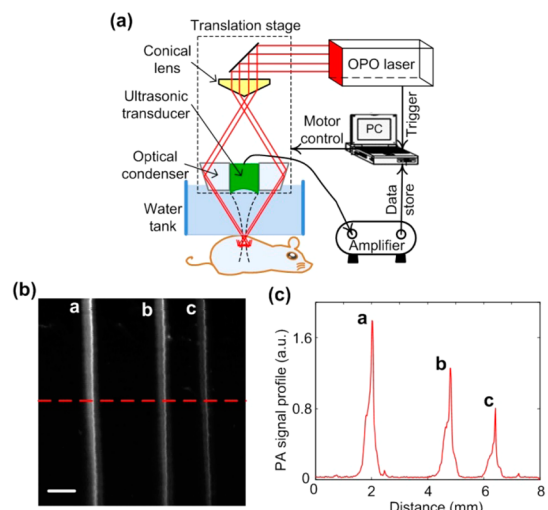


Figure 1. (a) Scheme of the PAM system used for *in vivo* animal imaging. (b) MIP image of three pieces of horse hair obtained by the PAM system. Scale bar = 1 mm. (c) Image profile along the red dashed line from part b.

Enhanced tumor uptake of the nanodrug was facilitated by the efficient delivery vehicle. Meanwhile the detection specificity and sensitivity also significantly benefited from the GO accumulation in the tumor. Resolution-scalable PAM was developed to evaluate the treatment progress and compare the therapeutic efficacy by different drug delivery strategies. Our results demonstrated that the PAM system offers much deeper imaging penetration than optical imaging methods, allowing early-stage and sensitive detection of tumor angiogenesis and therapeutic evaluation onset. This prognosis method aided by synergistic nanodrugs might potentially spare patients from unnecessary suffering in an ineffectual chemotherapy course, resulting in a change to a new treatment course if necessary, and could ultimately impact the survival rate.

RESULTS

The schematic of our homemade PAM system (nanoPAM Inc.) is depicted in Figure 1a. Briefly, the light source was supplied by a tunable optical parametric oscillator laser pumped by a Q-switched Nd:YAG laser (Surelite I20, Continuum) with a 20 Hz pulse repetition rate. The laser wavelength is tunable from 410 to 2500 nm. In this study, 680 nm was chosen as the excitation wavelength for PA imaging acquisition. The laser beam, formed by a spherical conical lens, was converted to a ring shape and then focused by an optical condenser on mouse skin for PA signal generation. The incident laser pulse energy was $\sim 5 \text{ mJ/cm}^2$, well below the American National Standards Institute (ANSI) safety standard of 20 mJ/cm^2 .³⁰

As illustrated in Figure 1a, the animal was placed underneath a thin clear plastic membrane of a water tank that has a $4 \times 4 \text{ cm}^2$ opening.³¹ Produced acoustic pressures were detected by a single-element ultrasonic

detector (NDT Olympus) coaxially aligned with the laser-focused point. The transducer is replaceable by different alternatives such as a 20, 10, or 5 MHz detector for resolution-scalable imaging. A computer controls the two-dimensional translation stage for raster scanning of the subject through the opening. The PA data were first amplified by a low-noise signal amplifier (5072PR, Olympus) and then transferred to a high-precision data acquisition (DAQ) card (CS1422, Gage Inc.) in the computer for postprocessing. Light fluence measurement of the laser pulse from a photodiode (DET110, Thorlabs) was employed to trigger PA data collection and signal compensation for pulse-to-pulse fluctuations of laser energy. This PAM system features high imaging sensitivity and resolution scalability.

To characterize the PAM system, three pieces of horse hair fiber with a diameter from 40 to 90 μm were imaged by a 20 MHz ultrasonic transducer. The horse hair was embedded and stabilized in agar with a thickness of ~1 mm, resembling scattering tissue. The optical absorption distribution of the hair is displayed in a maximum intensity projection (MIP) image with high contrast in Figure 1b. The image profiles along the red dashed line from the MIP image (Figure 1b) are plotted in Figure 1c, where the three sharp peaks correspond to the hair fibers. The full width at half-maximum (fwhm) of the imaged object was calculated to be ~50 μm , which agrees well with the theoretical calculation of spatial resolution in the frequency domain.³² The results demonstrate that the system can resolve micrometer-scale structure with high contrast.

The synthetic procedure of the nanoformulation is briefly illustrated in Figure S1 (see details in the Supporting Information). First, uniform GO nanoparticles were prepared from graphite based on a modified Hummer's method.^{33,34} Eight-amino-terminated poly(ethylene glycol) (5 kDa) was conjugated with the carboxylic groups of GO via amide formation to obtain GO-PEG. Then PEG-GO was labeled by Cy5.5 probes by amino and carboxyl group reaction. Afterward, a large amount of Dox was stacked on the GO surface via $\pi-\pi$ stacking. To verify each step of the synthesis process, UV-vis-NIR spectra of the four agents (GO, Dox, GO-Cy5.5, and GO-Cy5.5-Dox) were obtained, as shown in Figure 2a. The blue line representing GO-Cy5.5 exhibited two characteristic absorption peaks at 230 and 680 nm, indicating the labeling of Cy5.5 on GO. The absorption spectra of GO-Cy5.5-Dox (red line) exhibited three absorption peaks at 230, 480, and 680 nm, respectively, suggesting successful conjugation of three components. The loading capacity of Dox to GO vehicles was ~133.32 wt % by calculation (Figure S4).³⁵

Atomic force microscopy (AFM) images depicted the particle size of GO-PEG in Figure S2a. For statistical study, 5668 visualizations were randomly chosen to detail the particle size distribution including the

thickness, area, and volume of the three nanosheets in Figure S3. After labeling with Cy5.5 dye, the thickness of the GO-Cy5.5 nanoparticles increased to ~2 nm. Furthermore, the thickness of GO-PEG-Cy5.5-Dox increased more significantly, shown by the height profile plotted in Figure S2d and the height distribution in Figure S3a. Moreover, the surface area and particle volume of the nanosheets were evidenced, as shown in Figures S3b and c. This morphological change is mainly attributable to the large stacking of small Dox molecules on the surface of GO nanosheets. The fluorescence emission curves of GO-Cy5.5-Dox under the 480 and 680 nm excitation, respectively, are shown in Figure 2b. Under 680 nm excitation, a significant peak at 695 nm appeared in the emission curve due to the existence of Cy5.5, while under 480 nm the emission peak was found to be 520 and 590 nm, which is due to the GO nanosheets. In our study, 680 nm was chosen as the excitation wavelength to trace the distribution of nanoformulation pharmacokinetics in the whole body of the mice.

The absorbance of GO-Cy5.5-Dox agents is in a linear relationship with the concentrations, as shown in Figure S4. Since the signal-to-noise ratio (SNR) of the PA signals is proportional to the optical density,³⁶ accumulation of the highly absorbing nanoparticles can be used to improve the imaging contrast. Mice bearing H1975 lung adenocarcinoma were intravenously (iv) injected with either GO-Cy5.5-Dox (200 μL , Dox concentration at 8 mg/kg) or phosphate-buffered saline (PBS) (200 μL). A volume of $9 \times 9 \times 4 \text{ mm}^3$ of the tumor before and after the injection was scanned with a 10 MHz transducer. The PA image before injection (Figure 2c) revealed the main blood vessels, but the local tiny structures were almost invisible with low resolution. Six hours after GO injection, the vascular network with defined architecture was clearly visible, as shown in Figure 2d. The microvessels (indicated by white arrows) in the imaging region were significantly boosted in contrast. For quantitative comparison, we selected an identical region-of-interest marked by the dashed square area in both PAM images before and after GO injection. In the control group, the PAM image after PBS injection (Figure 2f), which mainly maps coarse vessels, was similar to that before injection (Figure 2e). A two-tailed Student's *t* test was used to reveal the variation of these two groups ($n = 4/\text{group}$). The image contrast after GO addition was enhanced 2.1 ± 0.2 times via calculation, compared with unchanged contrast in the PBS group. The statistical image differences also implied that the injected GO-Cy5.5-Dox agents were effectively enriched in the tumor region.

To study *in vivo* behavior of the nanodrugs, we measured the blood circulation dynamics by recording fluorescence signals of Dox at different time points. All fluorescence imaging and signal analysis

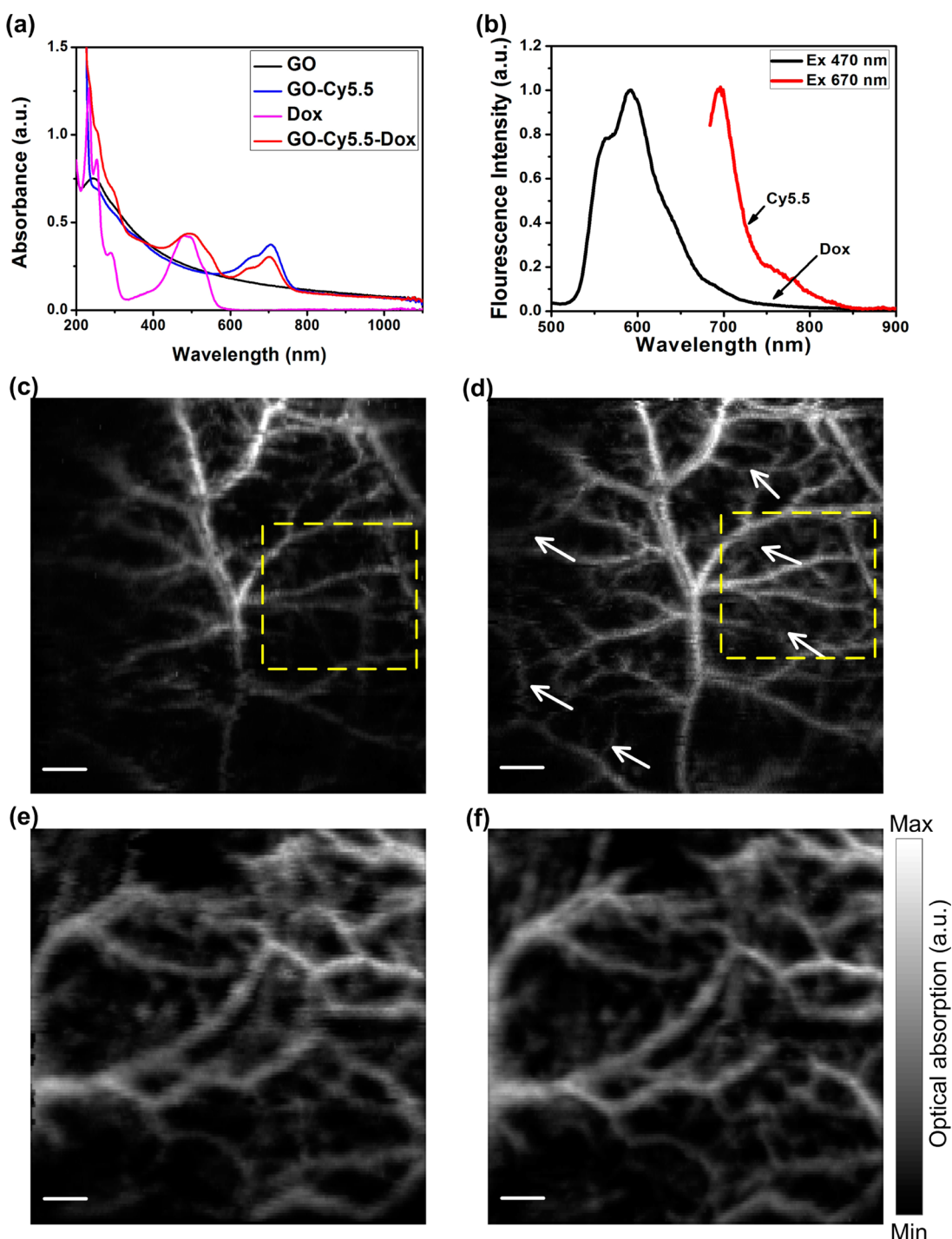


Figure 2. (a) UV-vis-NIR of GO, GO-Cy5.5, Dox, and GO-Cy5.5-Dox, respectively. (b) Fluorescence spectra of GO-Cy5.5-Dox excited at 480 nm (black) and 680 nm (red), respectively. (c) MIP image of tumor supply vessels before injection of GO-Cy5.5-Dox. (d) MIP image of tumor supply vessels 6 h after injection of GO-Cy5.5-Dox. (e) MIP image of tumor supply vessels before injection of PBS. (f) MIP image of tumor supply vessels 6 h after injection of PBS. Scale bar = 1 mm.

was carried out on a commercial Maestro optical imaging instrument (Caliper Life Sciences, Hopkinton, MA, USA). GO-Dox-Cy5.5 (200 μ L, Dox concentration at 8 mg/kg) was administered to an H1975 tumor bearing nude mouse by tail vein injection. Approximately 20 μ L of blood was iv drawn from the nude mouse. The drawn blood samples were subsequently excited at 500–720 nm (Dox spectrum, Figure 2b)

and then analyzed. As can be seen in Figure 3a, no fluorescence signal was detected in the blood before injection, while a strong signal emerged 3 min after injection and decreased gradually in time, indicating good circulation of GO-Cy5.5-Dox nanoparticles in the bloodstream. Specifically, the fluorescence signal in the blood 3 h after iv injection was 5.2 ± 0.3 -fold weaker than that at 3 min

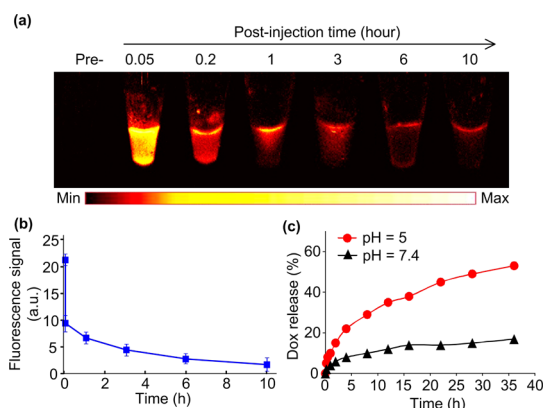


Figure 3. (a) Blood circulation of GO-Cy5.5-Dox in mice by tail vein injection. Blood samples of $5\ \mu\text{L}$ were collected at indicated time points into Eppendorf tubes for fluorescence imaging. (b) Fluorescence signal curve quantified from part a ($n = 4/\text{group}$). (c) *In vitro* drug release measurement of GO-Cy5.5-Dox in various pH conditions.

and 3.3 ± 0.1 -fold greater than that at 10 h ($n = 4/\text{group}$, Figure 3b).

In a mechanistic study, Dox released from the GO vehicle was tested in pH 5.0 buffer (modeling tumor environment) and pH 7.4 buffer (modeling normal physiological environment), respectively, as shown in Figure 3c. The solution was stored in an incubator shaker under constant stirring at 37°C , which was then sampled at various time points for dynamic release test. The free Dox was separated by centrifugation (100 kDa) at 10 000 rpm for 15 min and then quantified by UV-vis-NIR measurement. The results in Figure 3c show that much more Dox was released in the acid environment than that in the neutral environment. This phenomenon is attributable to the enhanced solubility and hydrophilicity of Dox in the acid environment.³⁷

To trace the kinetics of the nanoformulation in the mouse body, we investigated the tumor accumulation profile of GO-Cy5.5-Dox by fluorescence imaging (Figure 4a). After iv injection, GO-Cy5.5-Dox began to gather in the liver and spleen in the first 2 h, but gradually accumulated in the tumor with a strong fluorescence signal. Six hours after injection, the GO-Cy5.5-Dox mouse demonstrated dramatically greater fluorescence intensity in the tumor area (upper panel in Figure 4a), as opposed to the relatively low fluorescence signal in the Cy5.5-Dox group (lower panel), suggesting high tumor uptake efficiency of Dox by the nanocarriers. The background fluorescence signal does not cover the whole mouse at 48 h because only a small portion of the probes remained in the bloodstream and most of them were gradually taken up by the organs.

Another mouse group injected with GO-Cy5.5-Dox were euthanized at 48 h postinjection. Optical imaging of the major organs and tumor is shown in Figure 4b. A very strong fluorescence signal in the tumor

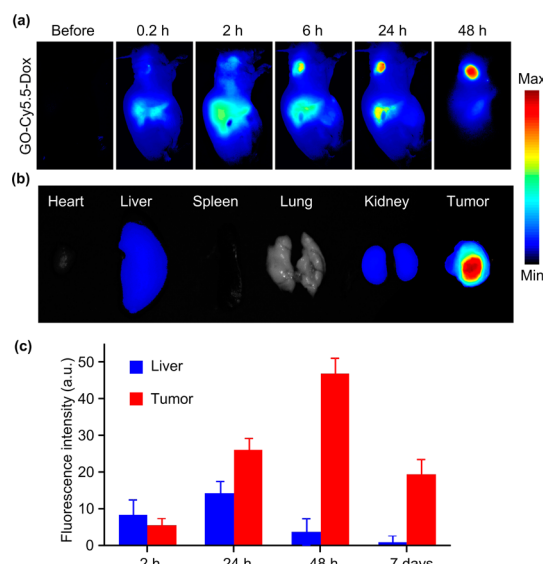


Figure 4. (a) Fluorescence imaging of GO-Cy5.5-DOX distribution *in vivo* in H1975-tumor-bearing mice. (b) Fluorescence imaging of major organs and tumor collected 48 h after drug injection. (c) Fluorescence signal of liver and tumor in mice at different time points by measuring the Cy5.5 fluorescence signal ($n = 5/\text{group}$).

was detected; however the organs, for example, liver and kidney, delineated much weaker fluorescence intensity. The uptake of GO in the liver may be underestimated if the tracer was partially degraded due to fluorescence loss of the metabolites. Liver and tumor from other mice groups were harvested to measure the Cy5.5 fluorescence signal of GO-Cy5.5-Dox at different time points ($n = 5/\text{group}$), as shown in Figure 4c. The biodistribution fluorescence measurements indicate that much more nanoparticles accumulated in the tumor than in the liver. The signal decrease in the liver may imply that nanoparticles accumulated in the liver were cleared gradually 7 days after injection. The nanoparticle accumulation in different organs depends on the size dimension, surface modification, functionality design, and its biodegradability, which requires further systematic investigations.

Two doses (one day apart) of either Dox or GO-Dox were iv injected into the mice at the same Dox concentration of $8\ \text{mg}/\text{kg}$ when the H1975 tumor size was $\sim 100\ \text{mm}^3$. A 20 MHz ultrasonic transducer was used to image an area of $4 \times 3.5\ \text{mm}^2$ on the tumor. Right after the first administration, vasomotion response was continuously monitored (day 0, 3, 6, and 9), as shown in Figure 5a. In the signal graph, the postinjection signal strengths were normalized by the initial value in each group to compare the change trend, as shown in Figure 5b. The PA images in the Dox group of Figure 5a showed that the PA signal of the coarse vessels remained almost unchanged with a slight signal decrease. In contrast, the vasculature progression, especially the small blood vessels, in the GO-Dox group was greatly inhibited on day 6 owing to

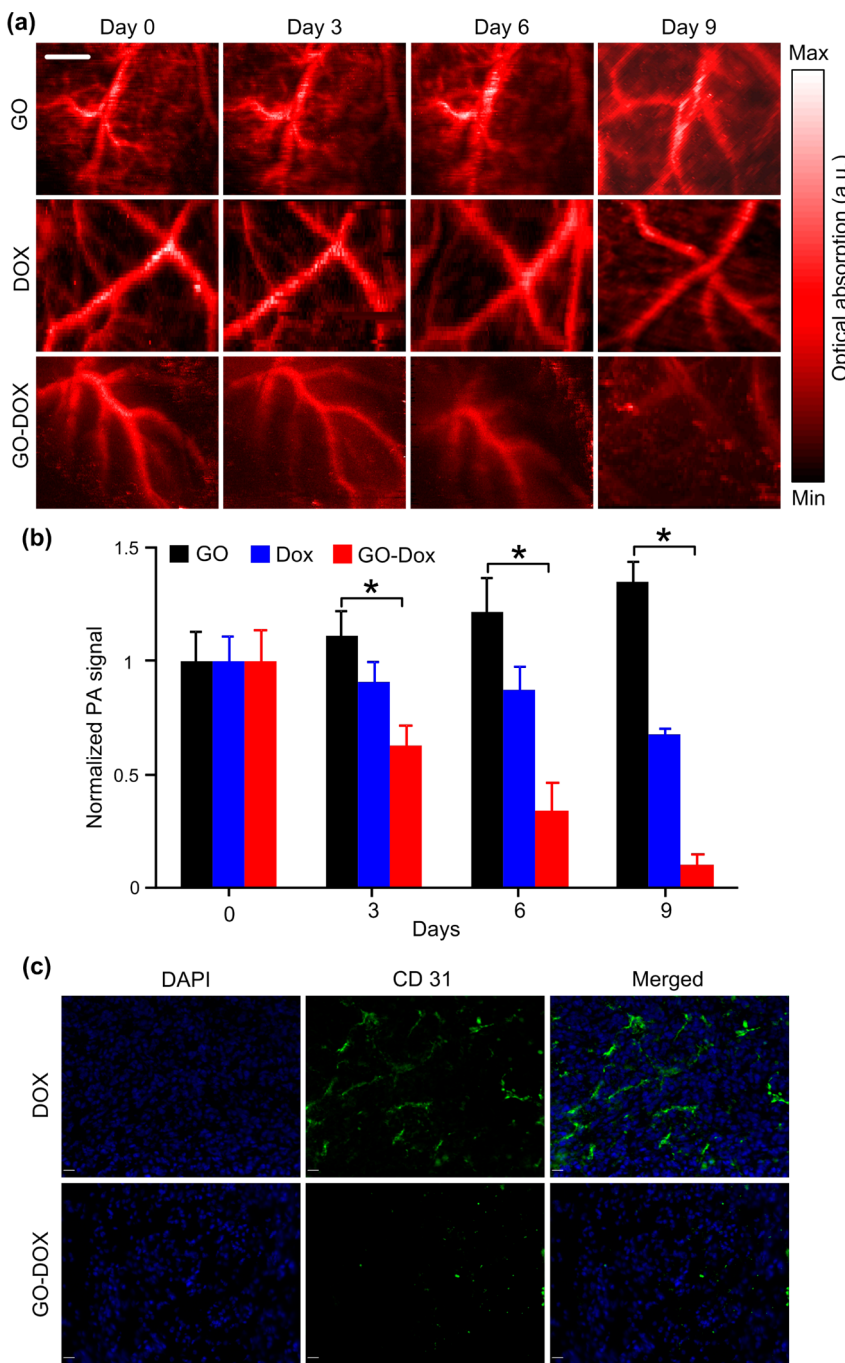


Figure 5. (a) Representative MIP images of a region-of-interest in tumor receiving GO treatment, Dox treatment, and GO-Dox treatment, respectively, at different time points. Scale bar = 1 mm. (b) Quantitative PA signals of blood vessels inhibited by the treatments ($n = 6$ /group). * $p < 0.01$. (c) CD31 immunohistochemical histology of the tumor section 6 days after treatment with Dox and GO-Dox chemotherapy. Scale bar = 20 μ m.

the high accumulation of Dox agents by the nano-carrier. These results suggest that PAM aided by GO may greatly improve visualization of the chemotherapeutic process at the early stage.

The results offered by PAM were much earlier than the tumor response measurement by conventional PA imaging (Figure 6a and tumor growth curve in Figure 7a). Statistical significance between the three groups ($n = 6$ in each group) was analyzed by Student's *t* test at each time point (Figure 5b). Quantitatively, the

treatment efficacy was improved 6.5 times over the control Dox group, shown in Figure 5b, suggesting the significantly higher tumor uptake efficiency of the nanoformulation. Even if all the injected nanoparticles were diffused away from the tumor at day 9, the PA signal decrease of the GO-Dox group was still ~ 3.1 times (6.5/2.1, 2.1 was the enhanced part by GO) lower than that of the Dox group.

To further verify that the PA signal reduction is caused by an antitumor effect of the chemotherapeutic

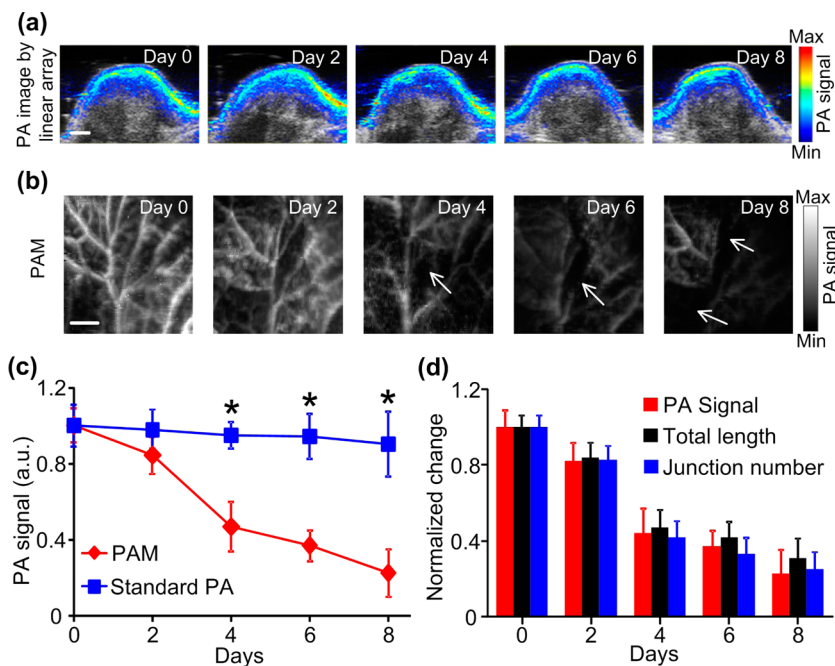


Figure 6. (a) Photoacoustic imaging of the tumor receiving chemotherapy by the conventional PA tomography system (VisualSonics). Scale bar = 1 mm. (b) Photoacoustic imaging of the tumor receiving chemotherapy by the PAM system. Scale bar = 1 mm. (c) PA signal change on the tumor measured by the conventional PA system and home-built PAM system ($n = 6$ /group). * $p < 0.01$. (d) PA signal, total length, and junction number of the vasculature from PAM images ($n = 6$ /group).

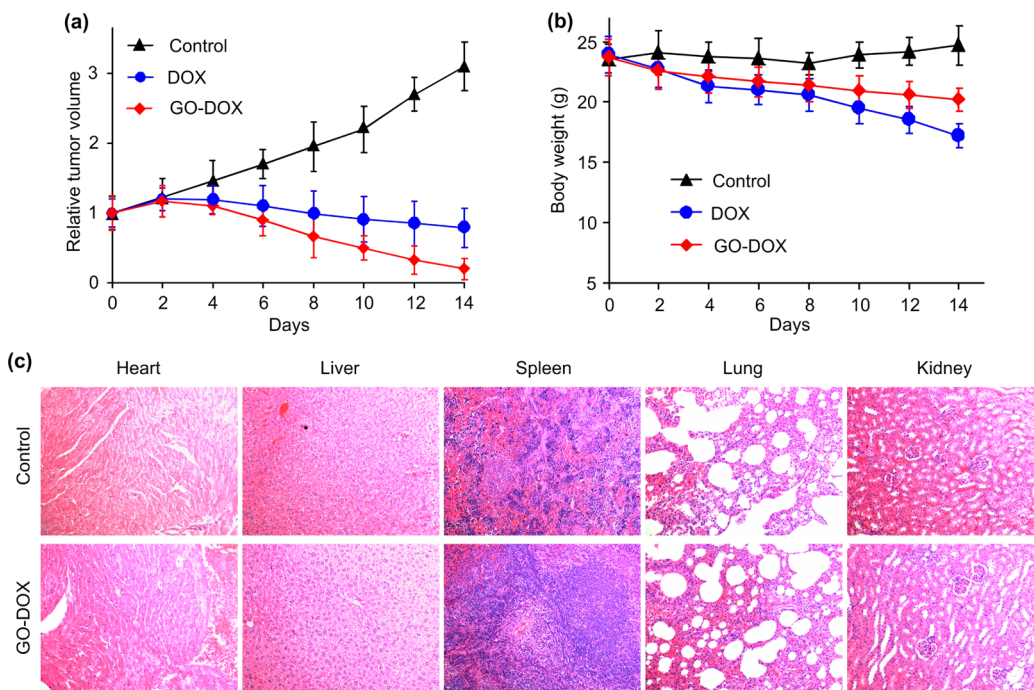


Figure 7. (a) Relative tumor volume of untreated and Dox- and GO-Dox-treated mice. (b) Body weight curves of the mice in the untreated and Dox- and GO-Dox-treated groups. (c) HE staining (10-fold magnification) of the major organs 1 week after PBS or GO-Dox (Dox concentration at 8 mg/kg) injection.

drug, blood vessels from frozen sections of tumors 6 days after therapy were stained by anti-CD31 antibody (green fluorescence). The CD31 staining protocol was described in previous literature.³ Numerous blood vessels are shown in the sections of the control group (Dox) in Figure 5c. In contrast, a remarkable

decrease in neovessels was found in the GO-Dox tumors. Quantitative results demonstrate 33 ± 4 vessels in the Dox group, compared with 11 ± 5 vessels in the GO-DOX group ($p < 0.01$), indicating the chemotherapy remarkably suppressed tumor angiogenesis.

To demonstrate the early-stage monitoring ability, our custom-built PAM was further compared with a conventional PA imaging instrument. A widely available commercial PA imaging system (VeoLAZR2100, VisualSonics) was utilized for imaging as control. A transducer array (central frequency 21 MHz) was applied for image acquisition. Light at 680 nm from a wavelength-tunable laser was used to excite PA signals. Filtered back-projection was utilized for photoacoustic tomography (PAT) image reconstruction.^{38,39} PAT and ultrasound images were captured separately and superimposed in one image. After the second dose injection of GO-Dox (Dox concentration at 8 mg/kg), therapeutic response was monitored by both our PAM and the VisualSonics system, as shown in Figure 6.

The cross section PA images from the VisualSonics system in Figure 6a representing the sagittal plane for centrally located tumor showed that the tumor shape with the PA signal decreased slightly on day 8. Unlike the PAM imaging system, the linear transducer array mainly supplies the physical morphology instead of imaging deliberate structure such as microvessels.⁴⁰ In contrast, the PAM results in Figure 6b clearly manifest that the angiogenic vessels were greatly suppressed on day 4. At each time point, a two-tailed Student's *t* test was applied to evaluate the variation of the two groups. The 4 days earlier (at least) detection difference in Figure 6c indicates that the PAM system is sensitive enough to capture subtle changes of the chemotherapy response during the treatment course. Moreover, the normalized changes of the PA signal, total length, and interconnectivity analysis of the vascular network from Figure 6b are shown in Figure 6d. The total length and junction number of the vasculature confirm the chemotherapeutic depression trend shown in the PAM images. Specifically, compared to PA signals, the total vascular length represented by black columns exhibited later therapeutic signs, while the junction number represented by blue columns showed slightly earlier signs.

In general, injected agents need to circulate and extravasate the vascular compartment, circumvent reticuloendothelial system (liver and spleen) uptake, and be delivered to the desired site for therapeutic purposes. Tumor microenvironment is slightly acidic in comparison with normal tissues.⁴¹ The drugs loaded on the nanocarrier surface by stimulus-responsive stacking conjugation would be released in response to the external tumor microenvironment, as evidenced in Figure 3c.⁴² The physical size measurements of the tumor in Figure 7a, although reflected later pathological information than the PAM monitoring, confirmed better chemotherapeutic efficacy of the GO-Dox group over Dox and untreated groups.

The *in vivo* body weight curve in Figure 7b shows that the body weight of the GO-Dox mice group

dropped less than that of the Dox mice group. In the drug delivery, the GO-Dox nanoformulation is less toxic to the normal tissue than Dox due to the good biocompatibility of GO. In addition, more Dox agents in the form of GO-Dox accumulated in the tumor than sole Dox agents. Thus, after GO loading, fewer Dox agents were deposited in the normal tissue, resulting in less systematic toxicity. *Ex vivo* hematoxylin and eosin (H&E) histology (10-fold magnification) of major organs was implemented for nontoxicity validation of GO-Dox (Figure 7c). Higher magnification (40-fold) H&E histology images of liver and spleen are also illustrated in Figure S5. No obvious sign of organ damage was seen in the HE slides, indicating *in vivo* application potential of GO. It is also noteworthy that despite the high accumulation in the reticuloendothelial system in the first-day fluorescence imaging (Figure 4a), no obvious deformity was found in the organs after histological staining.

DISCUSSION AND CONCLUSIONS

Tumor supply vessels increase oxygen and other factors to cancer cells and expedite tumor expansion and metastasis, which is a key criterion of disease aggression or inhibition.^{43,44} Tumor neovascularization level is a superb criterion to evaluate the metastatic potential and monitor chemotherapy response. Therefore, neovasculation imaging is essential to assess tumor behavior, forecasting the treatment response, changing the therapy strategy if necessary, and ultimately maximizing the therapy effect. Benefiting from the exquisite sensitivity of PAM and the signal amplifying effect of synergistic nanotheranostics, we improved the imaging prognosis strategy with earlier outcomes and better image quality. In our study, a deeper imaging depth can be obtained by using a longer laser wavelength and a lower frequency ultrasound transducer at the expense of resolution worsening.⁴⁵ By adjusting the observation scale, versatile PAM is capable of imaging neovascularization and segment microvessel architecture responses to angiogenesis inhibitors, enabling tumor angiogenesis and treatment monitoring.

By using GO-Dox, we successfully amplified the image contrast for tumor neovascularization visualization, providing high detection sensitivity and imaging specificity. Moreover, the high loading capacity of the nanovehicle on the surface permits significantly effective chemotherapy, which can be continuously monitored by PAM. In our PAM experiments, the data collection conditions such as pulse energy, signal amplification, and DAQ card setting were maintained under the same parameters. Thus, the images acquired by the same transducer are comparable between figures. In our results, the PAM system aided by GO-Dox can detect obvious PA signal variation on tumor as early as 4 days after the treatment initiation,

while conventional PA imaging or the tumor growth curve reflects reduction until 5 days later. Consequently, combining PAM with GO-Dox allows tumor angiogenesis imaging inhibition and therapy response monitoring in a synergistic theranostic platform.

Compared with fluorescence imaging, PAM promises much higher spatial resolution since ultrasound pressure was much less scattered than photons in

tissue. In addition, PAM does not require undesirable fluorescent labeling since all contrast origins can potentially be detected at appropriate wavelengths by PAM, whereas only a few subsets of molecules in biological tissues are fluorescent. By upgrading the light source to a more portable laser with a kHz repetition rate, our system is highly translatable to bedside clinics and operation-room applications.

MATERIALS AND METHODS

Reagents. Unless otherwise noted, all solvents and compounds were purchased from Aldrich Chemical Co. (St. Louis, MO, USA). Cy5.5-NHS ester was purchased from GE Healthcare Life Science (Piscataway, NJ, USA). Doxorubicin (Adriamycin) was purchased from Doxil (ALZA Corporation, CA, USA).

Synthesis of GO-Cy5.5-Dox. GO-PEG was fabricated according to a modified Hummers method. Briefly, GO solution (1 mg/mL, 5 mL) and 25 mg of PEG were mixed. The solution was then sonicated for 15 min. *N*-(3-(Dimethylamino)propyl-*N*-ethylcarbodiimide hydrochloride (EDC) was added in two parts until 5 mM. After 12 h, excess PEG was washed with distilled water by a 100 kDa filter (Millipore Inc.). Then Cy5.5-NHS ester in DMSO was introduced to label the GO-PEG nanovehicles. The stability of GO-Cy5.5 was tested in standard bovine blood serum under constant stirring in 37 °C for 48 h, as shown in Figure S6. The possible released Cy5.5 was separated by filtration through a 3 kDa centrifugal filter. However, a very weak fluorescence signal was detected in the extracted solution, indicating relatively strong stability of GO-Cy5.5 in a biological system. Finally, 2 mL of Dox (1 mg/mL) was incubated with 1 mL of GO-Cy5.5 (1 mg/mL) for 24 h. Excess Dox was collected via centrifugation through a 100 kDa filter and rinsing 6–8 times. The concentration of the excess Dox was determined by the absorbance measurement at 480 nm using a calibration curve (Supplementary Figure S4). Thus, the amount of Dox loaded onto GO can be obtained by subtracting the unbound Dox from the total Dox amount initially added.

Animal Experiments. Immunodeficient female nude mice with a body weight of ~23 g were used for the animal study. Human H1975 adenocarcinoma cells (~10⁶ cells) were subcutaneously xenografted to the right shoulder of the mice. During the experiment, 1–2% isoflurane mixed with oxygen through a calibrated vaporizer was used for animal anesthesia. Guidelines on the care and the use of laboratory animals at Xiamen University and National Institutes of Health were followed for all animal handling.

H&E Staining. Tissue sections were harvested and immersed in 10% buffered formalin solution for 2 d and then transferred to 30% sucrose in PBS. Sections were then immersed in optimal cutting temperature media and frozen for 10 s in an isopentane bath that was placed in liquid nitrogen. Tissue sections (5 µm) were sliced and placed on glass slides and imaged with a bright-field microscope (Olympus).

Conflict of Interest: The authors declare no competing financial interest.

Acknowledgment. This work was supported by the National Science Foundation of China (81301257, 81371596, 51373144), the National Basic Research Program of China (973 Program 2013CB733802, 2014CB744503), and the Intramural Research Program (IRP) of the National Institute of Biomedical Imaging and Bioengineering (NIBIB), National Institutes of Health (NIH). The authors also acknowledge instrumental and technical support from nanoPAM Inc.

Supporting Information Available: Synthetic procedure, AFM characterization and analysis, optical properties, nontoxicity validation, and stability of the nanoparticles are provided. This material is available free of charge via the Internet at <http://pubs.acs.org>.

REFERENCES AND NOTES

1. Azim, H.; de Azambuja, E.; Colozza, M.; Bines, J.; Piccart, M. Long-Term Toxic Effects of Adjuvant Chemotherapy in Breast Cancer. *Ann. Oncol.* **2011**, *22*, 1939–1947.
2. Lynn, J. J.; Chen, K. F.; Weng, Y. M.; Chiu, T. F. Risk Factors Associated with Complications in Patients with Chemotherapy-Induced Febrile Neutropenia in Emergency Department. *Hematol. Oncol.* **2013**, *31*, 189–196.
3. Nie, L.; Wang, S.; Wang, X.; Rong, P.; Ma, Y.; Liu, G.; Huang, P.; Lu, G.; Chen, X. *In Vivo* Volumetric Photoacoustic Molecular Angiography and Therapeutic Monitoring with Targeted Plasmonic Nanostars. *Small* **2014**, *10*, 1585–1593.
4. Ghosh, P.; Han, G.; De, M.; Kim, C. K.; Rotello, V. M. Gold Nanoparticles in Delivery Applications. *Adv. Drug Delivery Rev.* **2008**, *60*, 1307–1315.
5. Mallidi, S.; Larson, T.; Tam, J.; Joshi, P. P.; Karpouli, A.; Sokolov, K.; Emelianov, S. Multiwavelength Photoacoustic Imaging and Plasmon Resonance Coupling of Gold Nanoparticles for Selective Detection of Cancer. *Nano Lett.* **2009**, *9*, 2825–2831.
6. Han, G.; Ghosh, P.; Rotello, V. M. Functionalized Gold Nanoparticles for Drug Delivery. *Nanomedicine (London)* **2007**, *2*, 113–123.
7. Bartczak, D.; Muskens, O. L.; Sanchez-Elsner, T.; Kanaras, A. G.; Millar, T. M. Manipulation of *in Vitro* Angiogenesis Using Peptide-Coated Gold Nanoparticles. *ACS Nano* **2013**, *7*, 5628–5636.
8. Dikin, D. A.; Stankovich, S.; Zimney, E. J.; Pineri, R. D.; Dommett, G. H.; Evmenenko, G.; Nguyen, S. T.; Ruoff, R. S. Preparation and Characterization of Graphene Oxide Paper. *Nature* **2007**, *448*, 457–460.
9. Yang, K.; Feng, L.; Hong, H.; Cai, W.; Liu, Z. Preparation and Functionalization of Graphene Nanocomposites for Biomedical Applications. *Nat. Protoc.* **2013**, *8*, 2392–2403.
10. Yang, K.; Zhang, S.; Zhang, G.; Sun, X.; Lee, S. T.; Liu, Z. Graphene in Mice: Ultrahigh *In Vivo* Tumor Uptake and Efficient Photothermal Therapy. *Nano Lett.* **2010**, *10*, 3318–3323.
11. Tian, B.; Wang, C.; Zhang, S.; Feng, L.; Liu, Z. Photothermally Enhanced Photodynamic Therapy Delivered by Nano-Graphene Oxide. *ACS Nano* **2011**, *5*, 7000–7009.
12. Sheng, Z.; Song, L.; Zheng, J.; Hu, D.; He, M.; Zheng, M.; Gao, G.; Gong, P.; Zhang, P.; Ma, Y.; Cai, L. Protein-Assisted Fabrication of Nano-Reduced Graphene Oxide for Combined *In Vivo* Photoacoustic Imaging and Photothermal Therapy. *Biomaterials* **2013**, *34*, 5236–5243.
13. Lalwani, G.; Cai, X.; Nie, L.; Wang, L. V.; Sitharaman, B. Graphene-Based Contrast Agents for Photoacoustic and Thermoacoustic Tomography. *Photoacoustics* **2013**, *1*, 62–67.
14. Wang, Y.-W.; Fu, Y.-Y.; Peng, Q.; Guo, S.-S.; Liu, G.; Li, J.; Yang, H.-H.; Chen, G.-N. Dye-Enhanced Graphene Oxide for Photothermal Therapy and Photoacoustic Imaging. *J. Mater. Chem. B* **2013**, *1*, 5762–5767.
15. Song, S.; Xiong, C.; Lu, W.; Ku, G.; Huang, G.; Li, C. Apoptosis Imaging Probe Predicts Early Chemotherapy Response in Preclinical Models: A Comparative Study with 18F-FDG PET. *J. Nucl. Med.* **2013**, *54*, 104–110.
16. Dunnwald, L. K.; Gralow, J. R.; Ellis, G. K.; Livingston, R. B.; Linden, H. M.; Specht, J. M.; Doot, R. K.; Lawton, T. J.;

- Barlow, W. E.; Kurland, B. F.; *et al.* Tumor Metabolism and Blood Flow Changes by Positron Emission Tomography: Relation to Survival in Patients Treated with Neoadjuvant Chemotherapy for Locally Advanced Breast Cancer. *J. Clin. Oncol.* **2008**, *26*, 4449–4457.
17. Benatar, N.; Cronin, B.; O'doherty, M. Radiation Dose Rates from Patients Undergoing Positron Emission Tomography: Implications for Technologists and Waiting Areas. *Eur. J. Nucl. Med.* **2000**, *27*, 583–589.
18. Grohn, O. H.; Valonen, P. K.; Lehtimaki, K. K.; Vaisanen, T. H.; Kettenm, M. I.; Yla-Herttula, S.; Kauppinen, R. A.; Garwood, M. Novel Magnetic Resonance Imaging Contrasts for Monitoring Response to Gene Therapy in Rat Glioma. *Cancer Res.* **2003**, *63*, 7571–7574.
19. Fellah, S.; Girard, N.; Chinot, O.; Cozzone, P. J.; Callot, V. Early Evaluation of Tumoral Response to Antiangiogenic Therapy by Arterial Spin Labeling Perfusion Magnetic Resonance Imaging and Susceptibility Weighted Imaging in a Patient with Recurrent Glioblastoma Receiving Bevacizumab. *J. Clin. Oncol.* **2011**, *29*, e308–e311.
20. Cook, J. R.; Frey, W.; Emelianov, S. Quantitative Photoacoustic Imaging of Nanoparticles in Cells and Tissues. *ACS Nano* **2013**, *7*, 1272–1280.
21. Zha, Z.; Deng, Z.; Li, Y.; Li, C.; Wang, J.; Wang, S.; Qu, E.; Dai, Z. Biocompatible Polypyrole Nanoparticles as a Novel Organic Photoacoustic Contrast Agent for Deep Tissue Imaging. *Nanoscale* **2013**, *5*, 4462–4467.
22. Pu, K.; Shuhendler, A. J.; Jekerst, J. V.; Mei, J.; Gambhir, S. S.; Bao, Z.; Rao, J. Semiconducting Polymer Nanoparticles as Photoacoustic Molecular Imaging Probes in Living Mice. *Nat. Nanotechnol.* **2014**, *9*, 233–239.
23. Wang, L. V.; Hu, S. Photoacoustic Tomography: *In Vivo* Imaging from Organelles to Organs. *Science* **2012**, *335*, 1458–1462.
24. Chen, Y. S.; Frey, W.; Aglyamov, S.; Emelianov, S. Environment-Dependent Generation of Photoacoustic Waves from Plasmonic Nanoparticles. *Small* **2012**, *8*, 47–52.
25. Wang, B.; Zhao, Q.; Barkey, N. M.; Morse, D. L.; Jiang, H. Photoacoustic Tomography and Fluorescence Molecular Tomography: A Comparative Study Based on Indocyanine Green. *Med. Phys.* **2012**, *39*, 2512–2517.
26. Patel, M. A.; Yang, H.; Chiu, P. L.; Mastrogiovanni, D. D.; Flach, C. R.; Savaram, K.; Gomez, L.; Hemnarine, A.; Mendelsohn, R.; Garfunkel, E.; *et al.* Direct Production of Graphene Nanosheets for Near Infrared Photoacoustic Imaging. *ACS Nano* **2013**, *7*, 8147–8157.
27. Liu, Z.; Robinson, J. T.; Sun, X. M.; Dai, H. J. PEGylated Nanographene Oxide for Delivery of Water-Insoluble Cancer Drugs. *J. Am. Chem. Soc.* **2008**, *130*, 10876–10877.
28. Chen, D.; Feng, H. B.; Li, J. H. Graphene Oxide: Preparation, Functionalization, and Electrochemical Applications. *Chem. Rev.* **2012**, *112*, 6027–6053.
29. Zhang, S. A.; Yang, K.; Feng, L. Z.; Liu, Z. *In Vitro* and *In Vivo* Behaviors of Dextran Functionalized Graphene. *Carbon* **2011**, *49*, 4040–4049.
30. American National Standard for Safe Use of Lasers ANSI Z136.1-2000; American National Standards Institute Inc., **2000**.
31. Li, W.; Sun, X.; Wang, Y.; Niu, G.; Chen, X.; Qian, Z.; Nie, L. *In Vivo* Quantitative Photoacoustic Microscopy of Gold Nanostar Kinetics in Mouse Organs. *Biomed. Opt. Express* **2014**, *5*, 2679–2685.
32. Xu, M.; Wang, L. V. Analytic Explanation of Spatial Resolution Related to Bandwidth and Detector Aperture Size in Thermoacoustic or Photoacoustic Reconstruction. *Phys. Rev. E* **2003**, *67*, 056605.
33. Hummers, W. S., Jr.; Offeman, R. E. Preparation of Graphitic Oxide. *J. Am. Chem. Soc.* **1958**, *80*, 1339–1339.
34. Stankovich, S.; Dikin, D. A.; Piner, R. D.; Kohlhaas, K. A.; Kleinhammes, A.; Jia, Y.; Wu, Y.; Nguyen, S. T.; Ruoff, R. S. Synthesis of Graphene-Based Nanosheets via Chemical Reduction of Exfoliated Graphite Oxide. *Carbon* **2007**, *45*, 1558–1565.
35. Sun, X.; Liu, Z.; Welsher, K.; Robinson, J. T.; Goodwin, A.; Zaric, S.; Dai, H. Nano-Graphene Oxide for Cellular Imaging and Drug Delivery. *Nano Res.* **2008**, *1*, 203–212.
36. Nie, L.; Ou, Z.; Yang, S.; Xing, D. Thermoacoustic Molecular Tomography with Magnetic Nanoparticle Contrast Agents for Targeted Tumor Detection. *Med. Phys.* **2010**, *37*, 4193–4200.
37. Liu, Z.; Sun, X.; Nakayama-Ratchford, N.; Dai, H. Supramolecular Chemistry on Water-Soluble Carbon Nanotubes for Drug Loading and Delivery. *ACS Nano* **2007**, *1*, 50–56.
38. Nie, L.; Cai, X.; Maslov, K.; Garcia-Uribe, A.; Anastasio, M. A.; Wang, L. V. Photoacoustic Tomography through a Whole Adult Human Skull with a Photon Recycler. *J. Biomed. Opt.* **2012**, *17*, 110506.
39. Park, S.; Karpouk, A. B.; Aglyamov, S. R.; Emelianov, S. Y. Adaptive Beamforming for Photoacoustic Imaging. *Opt. Lett.* **2008**, *33*, 1291–1293.
40. Nie, L.; Chen, M.; Sun, X.; Rong, P.; Zheng, N.; Chen, X. Palladium Nanosheets as Highly Stable and Effective Contrast Agents for *In Vivo* Photoacoustic Molecular Imaging. *Nanoscale* **2014**, *6*, 1271–1276.
41. Tannock, I. F.; Rotin, D. Acid pH in Tumors and its Potential for Therapeutic Exploitation. *Cancer Res.* **1989**, *49*, 4373–4384.
42. Cajot, S.; Van Butsele, K.; Paillard, A.; Passirani, C.; Garcion, E.; Benoit, J. P.; Varshney, S. K.; Jerome, C. Smart Nanocarriers for pH-Triggered Targeting and Release of Hydrophobic Drugs. *Acta Biomater.* **2012**, *8*, 4215–4223.
43. Hanahan, D.; Weinberg, R. A. Hallmarks of Cancer: the Next Generation. *Cell* **2011**, *144*, 646–674.
44. Barinaga, M. A Face-off over Tumor Blood Supply. *Science* **2000**, *287*, 783–785.
45. Nie, L.; Chen, X. Structural and Functional Photoacoustic Molecular Tomography Aided by Emerging Contrast Agents. *Chem. Soc. Rev.* **2014**, *43*, 7132–7170.